Hydrodynamic modelling of the tide propagation in a tropical delta: overcoming the challenges of data scarcity

Ignace Pelckmans[1], Olivier Gourgue[1,2], Jean-Phillipe Belliard[1], Luis E. Dominguez-Granda[3], Cornelis Slobbe[4], Stijn Temmerman[1]

[1] Ecosystem Management (ECOBE), University of Antwerp, Antwerp, Belgium
[2] Department of Earth & Environment, Boston University, Boston, USA
[3] Centro del Agua y Desarrollo Sostenible, ESPOL, Guayaquil, Ecuador
[4] Geoscience & Remote Sensing, TU Delft, Delft, The Netherlands
ignace.pelckmans@uantwerpen.be

Abstract—**Tropical river deltas are hotspots of human activity, but their vulnerability to flood risks is increasing due to sea level rise and worldwide conversion of mangroves, acting as natural buffers against marine flooding, into human land use. Moreover, extreme sea levels notably driven by climatic fluctuations such as the El Niño-Southern Oscillation, are projected to intensify with global warming. Hydrodynamic models offer a valuable tool in reaching a better understanding on the distribution of extreme sea levels in tropical deltas, but often their development is hampered by data scarcity. We combined state-of-the-art techniques to overcome that challenge by setting up a TELEMAC-2D model for the Guayas delta (Ecuador), a large (± 3,000 km²) delta with a complex geometry of branching river channels and mangrove forests. First, we used remote sensing to (1) obtain channel widths, which in turn determine the cell size in a flexible mesh, allowing us to capture both regional and local processes, (2) estimate intertidal flat topographies, and (3) delineate intertidal mangrove forests. Furthermore, we used an along-channel-coordinate interpolation to ensure channel connectivity in channels with scarce bathymetric observations. Finally, to capture the land-sea gradient in the water surface slope, we referenced all bathymetric and tide gauge data to a global geoid. Applying these techniques allows us to build a model which simulates tidal ranges (of 2 to 4 m) with an error ranging between 0.2 and 29 cm (i.e. 0.2 and 7.8 % of the observed tidal range), depending on tide gauge station. In a next stage, our model can be used to test how both El Niño and land use changes affect extreme sea levels in this tropical delta.**

I. INTRODUCTION

A. Coastal flooding in tropical deltas

Coastal deltas are highly vulnerable to flood risks which are very likely to increase in the near future [1]. Intensifying storms and climatic cycles such as the El Niño Southern Oscillation (ENSO) along with long-term sea level rise will trigger more frequent and more severe coastal floods [2,3,4] In addition, over 90 % of deltaic communities are located in developing countries with already dense populations expected to double before 2060 [5]. This increasing population pressure along with intensifying coastal hazards pose enormous risks to coastal communities, framing tropical deltas as communities which will be disproportionately hit by climate change [6].

B. Paper outline

Hydrodynamic models are valuable tools in understanding how extreme sea levels originate and propagate through deltas but especially in tropical areas, data scarcity often hampers the development of such models. This paper presents an integrated model setup where we combined several state-of-the art techniques to overcome the data scarcity challenge and setup a tidal model (no wind or short-period waves) model in the Guayas delta, Ecuador. The propagation of tides through a tropical delta is driven by ebb-and-flow currents in the open ocean but when these tidal waves enter the delta, geometric properties of tidal channels and vegetated wetlands, mangroves, govern deltaic hydrodynamics. In the first part, we describe how we used remote sensing and GIS-techniques to build an unstructured mesh in order to cover the multi-scale character of deltaic hydrodynamics. Secondly, we list two methods which were used to interpolate scarce bathymetric observations in order to ensure hydrodynamic connectivity over the entire domain. Thirdly, we stress the importance of using a vertical reference level which allows the model to include all major drivers, including a land-to-sea gradient. In the final section, we shed light on the calibration process of the channel's bottom friction and the mangroves forest floor elevation. The combination of these methods allowed us to build and calibrate a TELEMAC-2D model which in later stages will be used to further investigate the propagation of ENSO-driven extreme sea levels in a tropical delta.

C. Study area

The Guayas delta is the largest river delta along the Latin Pacific coast and flows into the Gulf of Guayaquil (Fig. 1). The gulf and delta are subject to semi-diurnal tides with a mean tidal range of ± 2 m at the SW seaward boundary of the gulf. When propagating landwards, the mean tidal range is amplified up to ± 5 m near the city of Guayaquil. Freshwater river discharge into the Guayas delta comes from the Babahoyo and Daule rivers in the North. Discharges vary strongly with values between 125 and 400 m³/s in the dry season (April – November) and values up to 1600 m³/s in the wet season (December – March) [7]. Similar to many other tropical deltas, the mangroves are heavily degraded after large parts of the delta were converted to aquaculture [8]. The tarnished ecosystem and its exposure to El Niño puts the delta under risk, a threat highlighted by a global study on risks of flood damage (relative to local GDP) in coastal cities, ranking Guayaquil on the 3rd highest place [9], highlighting the Guayas delta as a global hotspot of coastal hazards.

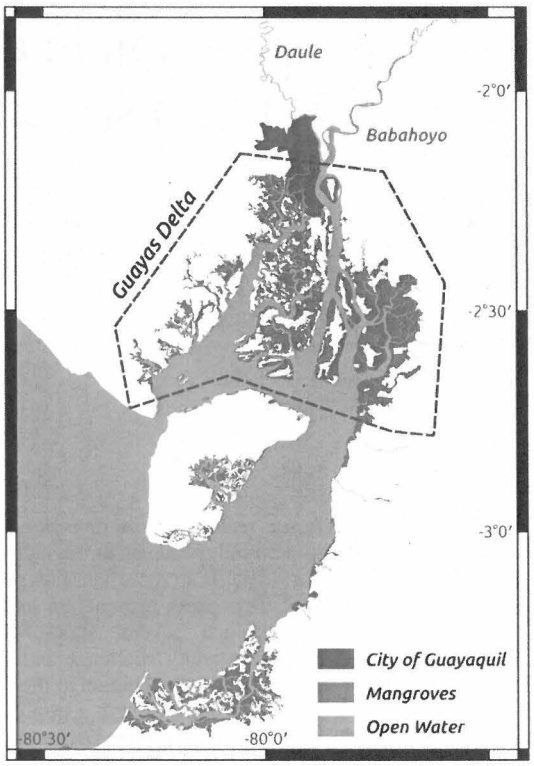

Fig.1: Map of the Gulf of Guayaquil, the western part of the domain containing the region of interest: the Guayas Delta. Both mangroves and open water are included in the model domain. The city of Guayaquil is not. The open ocean boundary is located east of the shown extent. Both freshwater boundaries are indicated (Daule and Babahoyo river).

II. Mesh Generation

A. Model domain

The domain of the model covers the entire Gulf of Guayaquil, stretching from the continental shelf at the open ocean (-81.25°) to 50 km upstream at the Babahoyo and Daule river from Guayaquil. The natural wetlands, mangroves, flood during high water levels and therefore, are included in the domain. After conversion to aquaculture, mangroves can no longer flood due to the construction of levees and therefore, aquaculture ponds are excluded from the domain.

B. Delineation of mangroves and channels

The use of satellite-borne remote sensing allowed us to delineate the mangroves and channels from aquaculture ponds, urban areas and surrounding agricultural land. ESA's Sentinel 2 is a collection of multi-spectral optical images which allows calculating the Normalized Difference Vegetation Index (NDVI) at a spatial resolution of 10 m. NDVI ranges from -1 to 1 with values above zero, indicating the presence of vegetation. In our study, mangroves were determined by pixels with a NDVI-value above a threshold value. To determine that value, we randomly selected 50 points in the mangroves and 50 points in other land cover types (e.g. aquaculture ponds, built-up areas, etc.). NDVI at all points in mangroves exceed the value of 0.6 while 49 of 50 in other land cover types did not. Consequently, mangroves were determined as all pixels with a NDVI-value > 0.6. To ensure channel connectivity, we applied a 1-pixel-wide dilation and erosion algorithm (Fig. 2). Afterwards, the entire domain was visually checked and compared with aerial pictures collected through Google Earth. If needed corrections were applied. Finally, manually delineated data of mangroves and channels for subareas within our study area were available through ESPOL, and after visual comparison, our NDVI-based results were considered satisfactory.

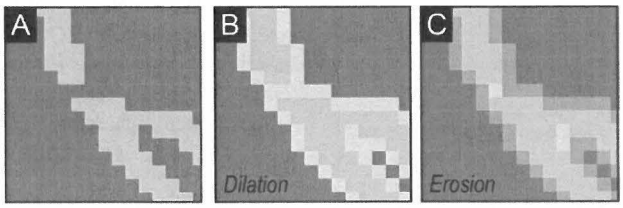

Fig 2.: (A) close up of original delineated channel (B) dilation process of 1 pixel wide (blue pixels) (C) erosion process after dilation, light green pixels indicate pixels which were removed again after erosion. Note how the channel kept its original width but is connected now.

C. Cell size

We constructed a mesh where cell sizes inside the delta are determined in function of the channel width. We developed a Python-based set of functions, '*tidealgeopro*' [10], to build a set of polylines representing the center line of the channel polygons (channel skeleton). In addition, as traditional stream order systems were insufficient because tidal channels do not have a clear flow direction, we developed a stream order system to rank all tidal channel segments (portion of channel in between the joining of tributaries) as illustrated in Fig. 3. To calculate channel width for each location in the channel, we first calculated the channel width for each vertex of the skeleton. Next, per segment, we applied a nearest neighbour interpolation to extrapolate the channel widths at the channel vertices to a raster (pixel size of 5m) in order to assign a channel width to each location in the channel. At tributary-joints, the interpolated channel-width rasters overlapped but priority was given to higher order streams. This resulted in a raster file representing channel width for all channels (Fig. 4A).

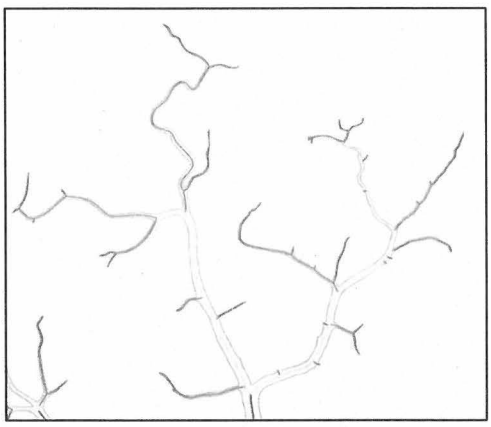

Fig. 3: Example of channel skeleton with colors representing stream orders per channel segment (green = 1, red = 2, yellow = 3, blue = 4).

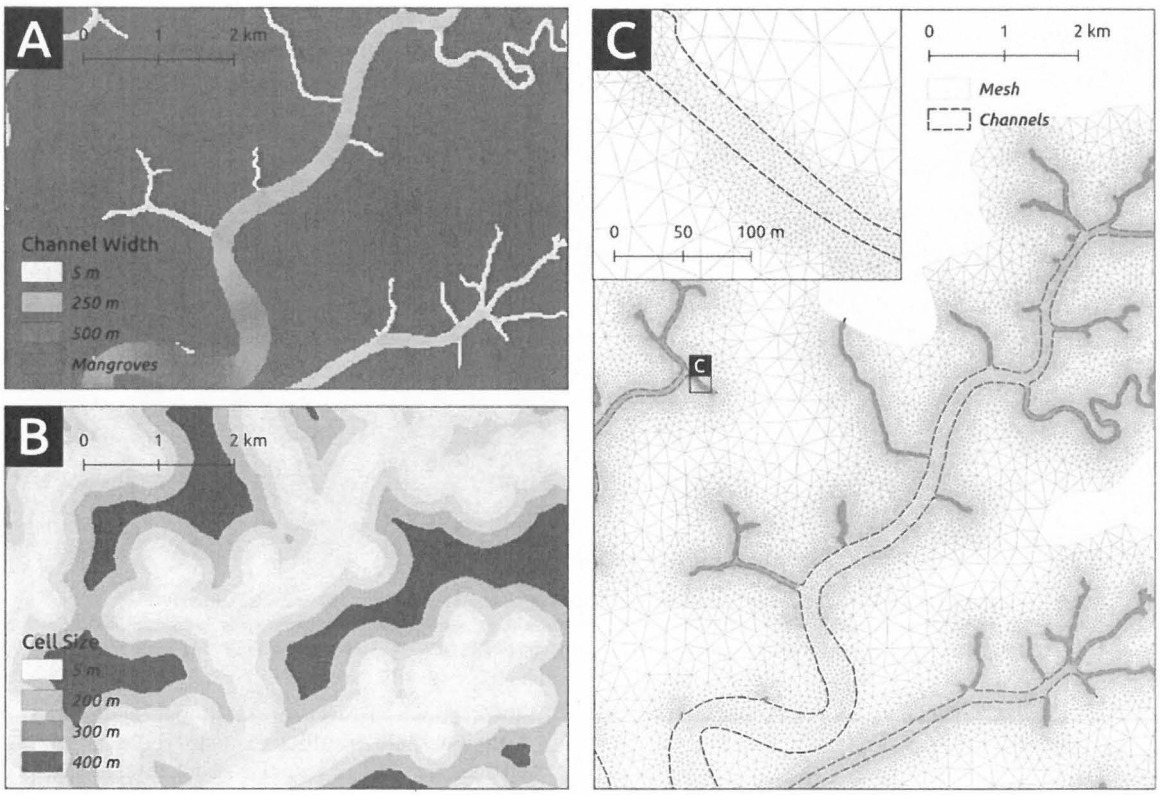

Fig. 4: (A) Example of channel width raster. (B) Example of raster file imposing the cell size of the eventual mesh (C) Example of mesh where the cell size has been calculated in function of the channel width.

Next, we expressed cell size in function of the channel width in order to ensure a minimum number (5) of mesh nodes broadwise. In addition, a minimum cell size of 5 m was enforced to limit the total number of elements. The cell size at the mangroves was set at 400 m. The latter might lead to strong gradients in cell size where narrow channels border mangrove forests, which could cause numerical instabilities. Therefore, we implemented stepwise buffers around the channels to impose smooth transitions in mesh cell size at the borders between channels and mangroves (Figure 4B & C). Cell sizes at the open ocean varied from 1000 m at the seaward boundary to 400 m at the entrance of the delta. The mesh was created using the finite element mesh generator GMSH [11].

III. Available Data

Water levels were obtained through 3 different sources: INOCAR shared water levels (1976 - 2019) from 8 tide gauge stations spread over the Gulf of Guayaquil, however many of the stations had significant gaps in the time series. Jan De Nul shared water levels from 11 tide gauge stations from which 10 are located along the main channels in the delta. Thirdly, water pressure sensors were installed at three different locations in the delta appr. 10 - 50 m inside the mangrove forests, permanently logging water depth since March 2019.

Bathymetry data at the open ocean were obtained from the General Bathymetric Chart of the Ocean (GEBCO, 2020). Limited bathymetric data inside the delta were shared by the Oceanographic Institute of the Navy (INOCAR) as well as nautical charts in JPG-format.

IV. Boundary Conditions

Boundary conditions at the seaward boundary were derived from the global tidal models TPXO9 [12]. Upstream river discharge data were obtained through INHAM. The available data did not cover the entire watershed of the Guayas river, but the available data was extrapolated by means of a linear precipitation-weighted interpolation with monthly precipitation data collected from OpenLandMap [13].

V. Bathymetry Interpolation

At the open ocean and major channels, bathymetry at the mesh nodes was derived by a linear TIN-interpolation of the available data. No bathymetric data covering intertidal flats were available. To interpolate the bathymetric data in the channels dissecting the mangrove forests, observations were too scarce to apply a simple linear TIN interpolation.

A. Intertidal flat topographies

Based on the nautical charts in JPEG-format and Sentinel 2 images, we delineated 20 zones covering significantly large (area > 40 km²) intertidal flats. Per zone, we collected a time series of all available cloud-free Sentinel 2 imagery through the Google Earth Engine. For each image, the Modified Normalized Difference Water Index (MNDWI) was calculated

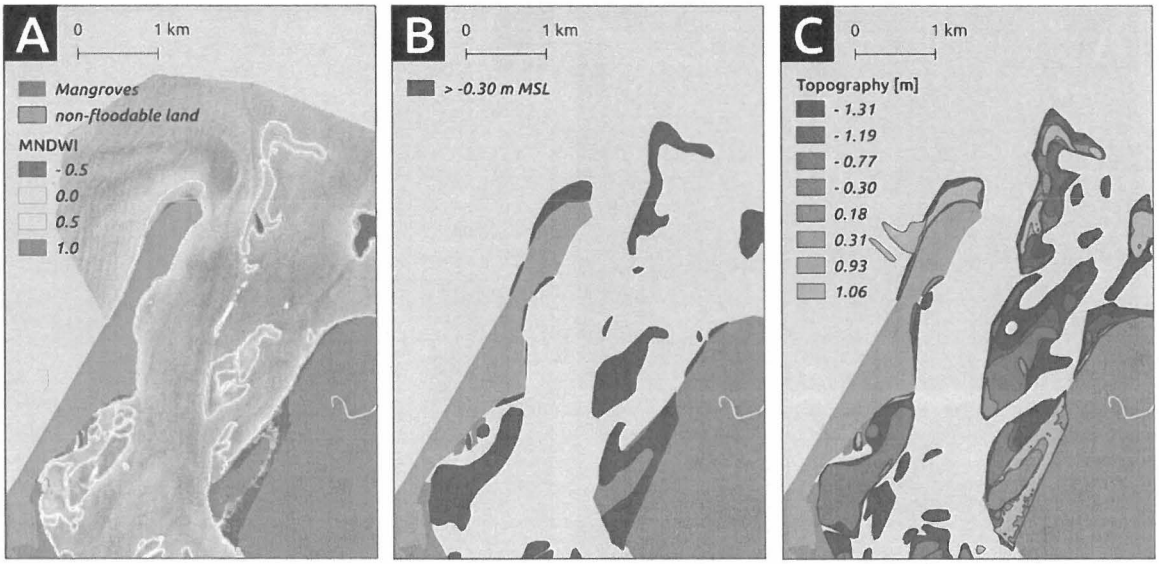

Fig. 5: (A) Modified Normalized Difference Water Index (MNDWI) of an intertidal mudflat. (B) Areas with MNDWI values lower than a given threshold, representing areas which were not submerged when a nearby tide gauge station measured a water height of 0.66 m below MSL. (C) Estimated topography of mudflat by combining MNDWI values at 4 different water heights.

(eq. 1), which ranges between -1 & 1 with positive values representing open water (Fig. 5A).

$$MDNWI = \frac{Green-SWIR}{Green+SWIR} \quad \text{(eq 1.)}$$

With *Green* and *SWIR* being the measured reflectance in the respectively, green part of the visible part of the electromagnetic spectrum and short-wave infrared part of the spectrum.

Submerged lands can be determined as cells with a MNDWI-index which exceeds a certain threshold value. Thus, the border between submerged and emerged cells is an estimation of the waterline at the timing of recording of that Sentinel 2 image [14, 15]. To define the value above which cells are considered submerged, we made use of an automatic thresholding technique called Otsu thresholding. In the latter, a threshold value is calculated to minimize intra-class variance (in our case of MNDWI) and maximize inter-class variance [16]. By obtaining the time of recording of each image, the obtained water lines could be linked to water levels of nearly located tide gauge stations. For instance, on Fig. 5B all areas which emerged when a nearby tide gauge station listed a water level of 0.66 m below mean sea level (MSL) are indicated by a red shade. The corresponding waterline can then be interpreted as contour lines of 0.66 m below MSL. By applying this algorithm for multiple Sentinel 2 images, acquired at different times and thus, different water levels, it is possible to build an estimated topography of an intertidal flat, as shown in Fig. 5C.

B. Channel bathymetry interpolation

Scarcely distributed point measurements of channel bathymetry were available to us, however, the resolution of the mesh strongly exceeded the resolution of the available observations, compelling an interpolation of the bathymetric observations. However, traditional cartesian interpolation techniques are insufficient. One could argue that the bed elevation within a channel is stronger related to its distance to the channel edge and position along the channel axis than its cartesian coordinates. Following this reasoning, we applied a linear TIN-interpolation after cartesian coordinates were projected to a channel fitted coordinate system [17]. Similar to section *II.C*, we first calculated the channel skeleton and divided the channel system into its different segments. On its turn, all bathymetry observations were assigned to a channel segment, which they were most closely located to.

Per segment and its related bathymetric observations, all cartesian coordinates of the bathymetry observations were projected to channel-fitted coordinates (see example in Fig. 6): (1) along-skeleton coordinate (*as*) which is the distance along the center line from the onset of the segment until the observation projected on the center line and (2) perpendicular-skeleton coordinate (*ps*) which is the distance from the observation to the center line. Such an approach conserves the geomorphic shape of a channel, even after interpolation. For instance, the interpolated channel bathymetry on the outside bends of channels will be more influenced by deep observations more down- and upstream than more closely located measurements at the inside bend.

VI. VERTICAL REFERENCE LEVEL

All collected data (bathymetry and tide gauge data) were referenced to the local mean sea level (MSL). However, when tidal waves enter and propagate through the delta, they are being pushed upwards, a process called tidal wave run-up. Along with significant freshwater river discharge, this creates a land-sea water surface slope in the MSL. Therefore, since MSL is derived from the hydrodynamics, it cannot act as an

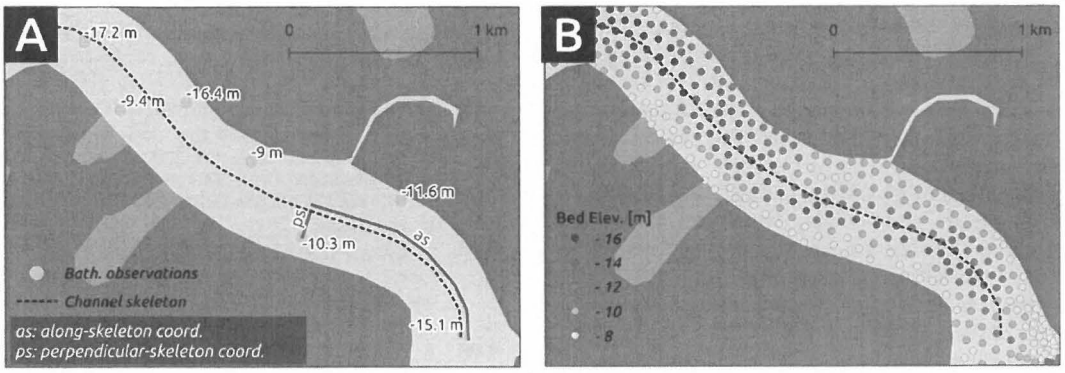

Fig. 6: (A) Example of channel segment with limited density of bathymetry observations (yellow markers). Channel coordinates are calculated as (as) the distance along the center line/skeleton measured from the start of that channel segment until each bathymetry observation projected on the center line and (ps) distance between the observation point and the center line. (B) Bathymetry of the channel segment after interpolation. Each marker represents a node on the final mesh. Nodes inside the mangrove forest are not shown.

independent reference level as it already includes an hydrostatic gradient from the ocean land inwards (Fig. 7). Therefore we referenced all data to a so-called geoid (XGM 2019). A geoid is a model describing an equi-potential gravitational field covering the entire globe. In other words, it is the shape which the ocean would take if the ocean's water level would only be governed by gravity and the rotation of the earth. Hence, if used as a vertical reference for hydrodynamic modelling, there would be no hydrostatic gradient between two locations with the same water surface level in reality as well [18].

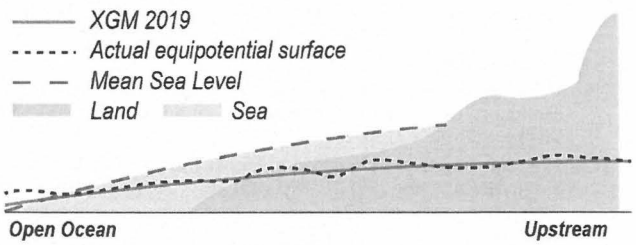

Fig. 7: Schematic representation of the geoid model (red line), the actual equipotential surface (black dashed line) and MSL (blue dashed line).

VII. Model Calibration

A. Mangroves forest floor elevation

No topographical data were available on the height of the mangrove forest floor. However, water depth measurements at the forest edge at three different locations, spread over the delta, were available. For instance, during the period 29th of September 2019 4:00:00 – 1st of October 2010 16:00:00, maximum water depths in the mangrove forest reached 60 cm, averaged over all three locations. Implicitly, we can estimate the mangrove forest floor elevation to be 60 cm lower than the high water mark surface in the mangroves. In other words, the mangrove forest floor elevation can be estimated based on the high water mark surface, however, the latter is affected by the mangrove forest floor elevation. Therefore, we set up an iterative process to estimate the mangrove forest floor elevation:

1. The first simulation excluded the mangroves from the floodable domain resulting in a high water mark surface which only included the channels. The high water mark surface was extrapolated to the mangroves by means of a 7th order polynomial surface and the mangrove forest floor elevation was set at this extrapolated high water mark minus 60 cm.
2. The updated mangrove forest floor was used as the input for a second simulation. This simulation resulted in a new high water mark, which did include the mangroves as the new mangrove topography allowed flooding in the mangroves since the forest floor elevation was set 60 cm below the high water mark in the channels.

   As all three surveyed locations are located near the border of the mangrove forest and channels, we can only assume that the forest floor is 60 cm below the high water mark at the edge of the forest. Hence, the newly updated elevation of the mangrove forest floor elevation was only set 60 cm lower than the high water mark at all nodes located on the border between mangroves and channels. Mangrove forest floor elevations inside the mangrove forest were again extrapolated by means of a 7th order polynomial surface.
3. On its turn, the resulting mangrove topography of the second simulation was used to simulate hydrodynamics, again resulting in a high water mark surface. The mangrove forest floor topography was updated by again, subtracting 60 cm for the last obtained high water mark and extrapolating the elevations to the inside of the mangrove forest. This iterative process was repeated until the RMSE of elevations at mangrove nodes between the two last iterations did differ less than 5 cm.

B. Channel bottom friction

Bottom friction in both the mangroves and open water areas is represented by the Manning's friction law. The dense network of aerial roots and branches in a mangrove forest adds

a significant amount of friction to the bottom friction and thus, an appropriate value of 0.14 was set as the Manning's friction coefficient *n*, based on previous studies (Zhang et al., 2012; Liu et al., 2014; Rhadarian & Niksokhan, 2017). One single value for the Manning's *n* was used to cover all open water areas, both the channels and the intertidal flats. To define this value, we ran model was with 7 different values for the Manning's n: 0.0050, 0.0075, 0.0100, 0.0125, 0.0150, 0.0175, 0.0200, 0.0225. Each simulation covered 60 hours and boundary conditions during a neap tide (the 5th of October 2019 22:00:00 - the 8th of October 2019 10:00:00, during which the mangroves do not flood) and a spring tide (the 29th of September 2019 4:00:00 - the 1st of October 2019 16:00:00). To evaluate each simulation, high and low water levels are compared at 11 separate stations spread over the delta. For both periods, simulated high and low water levels fitted best with observations, using a Manning's *n* of 0.0125. The time resolution of both the outputted model results and the observations were 5 minutes.

The model succeeded in simulating tidal propagation with errors in tidal range ranging from 2 mm to 24 cm (i.e. a relative error of 0.2 – 7.8 % of the observed tidal range). During the simulated spring tides, errors ranged from 15 cm to 39 (i. e. relative error of 4.4 – 8.73 % of the observed tidal range). Timing of high water levels and velocities did not contribute to the evaluation process.

VIII. CONCLUSION

Often, the development of hydrodynamic models is hampered by limited coverage of data on land use and topography & bathymetry. Here we have proven that the use of remote sensing and GIS-techniques such as waterline-extraction and channel-fitted coordinates could contribute in setting up a model, with relatively good agreement with observed water levels (errors on tidal range smaller then 9 % of the observed tidal range).

ACKNOWLEDGEMENT

We would like to thank the Research Foundation Flanders, Belgium for funding this research (FWO, PhD fellowship for fundamental research I. Pelckmans, 11E0721N).

REFERENCES

[1] J.W. Day, J. Agboola, Z. Chen, C. D'Elia, D. L. Forbes, L. Giosan et al. "Approaches to defining deltaic sustainability in the 21st century," Estuar. Coast. Shelf Sci., vol. 183, pp. 275–291, 2016.

[2] M. Oppenheimer, B. C. Glavovic, J. Hinkel, R. Van De Wal, A. K. Magnan, A. Abd-Elgawad et al. "Sea level rise and implications for low-lying islands, coasts and communities." In: IPCC Special Report on the Ocean and Cryosphere in a Changing Climate [H.-O. Pörtner, D.C. Roberts, V. Masson-Delmotte, P. Zhai, M. Tignor, E. Poloczanska, K. Mintenbeck, 2019.

[3] E. Kirezci, I. R. Young, R. Ranasinghe, S. Muis, R. J. Nicholls, D. Lincke and J. Hinkel "Projections of global-scale extreme sea levels and resulting episodic coastal flooding over the 21st Century." Sci. Reports 2020 vol 101 10, pp. 1–12, 2020.

[4] S. Vitousek, P. L. Barnard, C. H. Fletcher, N. Frazer, L. Erikson and C. D. Storlazzi "Doubling of coastal flooding frequency within decades due to sea-level rise." Sci. Reports 2017 vol 71 7, pp. 1–9, 2017.

[5] B. Neumann, A. T. Vafeidis, J. Zimmermann and R. J. Nicholls "Future coastal population growth and exposure to sea-level rise and coastal flooding - a global assessment." PLoS One vol 10, 2015.

[6] D. A. Edmonds, R. L. Caldwell, E. S. Brondizio and S. M. O. Siani "Coastal flooding will disproportionately impact people on river deltas." Nat. Commun., vol 111 11, pp. 1–8, 2020.

[7] INHAMI. Official INAMHI website. Accessed through http://www.serviciometeorologico.gob.ec/ on December 2019.

[8] S. E. Hamilton "Mangroves and aquaculture: a five decade remote sensing analysis of Ecuador's estuarine environments." Springer, 2019.

[9] S. Hallegatte, C. Green, R. J. Nicholls and J. Corfee-Morlot "Future flood losses in major coastal cities." Nat. Clim. Chang., vol 3, pp. 802–806, 2013.

[10] Gourgue, Olivier, Pelckmans, Ignace, Fagherazzi, Sergio, & Temmerman, Stijn. "ogourgue/tidalgeopro: Earth Surface Dynamics paper", 2021. accessible through: https://doi.org/10.5281/zenodo.5205285

[11] C. Geuzaine and J.F. Remacle "Gmsh: A 3-D finite element mesh generator with built-in pre- and post-processing facilities." International Journal for Numerical Methods in Engineering vol 79, pp. 1309–1331, 2007

[12] G. D. Egbert and S. Y. Erofeeva. "Efficient inverse modeling of barotropic ocean tides." Journal of Atmospheric and Oceanic Technology vol 19.2, pp. 183-204, 2002.

[13] T. Hengl "Monthly precipitation in mm at 1 km resolution based on SM2RAIN-ASCAT 2007-2018, IMERGE, CHELSA Climate and WorldClim (0.2)" accessible through https://doi.org/10.5281/zenodo.3256275, 2019.

[14] S. Sagar, D. Roberts, B. Bala, and L. Lymburner "Extracting the intertidal extent and topography of the Australian coastline from a 28 year time series of Landsat observations." Remote Sens. Environ., vol 195, pp. 153–169, 2017.

[15] J. U. Khan, M. D. N. Ansary, F. Durand, L. Testut, M. Ishaque, S. Calmant et al. "High-resolution intertidal topography from Sentinel-2 multi-spectral imagery: synergy between remote sensing and numerical modeling." Remote Sensing, vol 11 2888, 2019.

[16] R. Bishop-Taylor, S. Sagar, L. Lymburner, I. Alam and J. Sixsmith "Sub-pixel waterline extraction: characterising accuracy and sensitivity to indices and spectra." Remote Sensing, vol. 11 2984, 2019.

[17] V. Merwade, A. Cook and J. Coonrod "GIS techniques for creating river terrain models for hydrodynamic modeling and flood inundation mapping." Environ. Model. Softw., vol 23, pp. 1300–1311, 2008.

[18] P. Zingerle, R. Pail, T. Gruber and X. Oikonomidou "The combined global gravity field model XGM2019e." J. Geod., vol 94, 2020.